Lattice strain measurements using synchrotron diffraction to calibrate a micromechanical modeling in a ferrite–cementite steel

V. Taupin [a], R. Pesci [a], S. Berbenni [a,*], S. Berveiller [a], R. Ouahab [a], O. Bouaziz [b]

[a] Laboratoire d'Etude des Microstructures et de Mécanique des Matériaux, LEM3, CNRS, University of Lorraine/Arts et Métiers ParisTech, Metz Cedex 57045, France
[b] Arcelor Research, Arcelor Mittal, Maizières-les-Metz 57210, France

Keywords:
Synchrotron radiation
X-ray diffraction (XRD)
Dislocations
Carbides
Micromechanical Modeling

A B S T R A C T

In situ tensile tests were performed at room temperature on a ferrite–cementite steel specifically designed for this study. The evolution of the average stress in ferrite during loading was analyzed by X-ray diffraction. Lattice strain measurements were performed with synchrotron ring diffraction in both ferrite and cementite. These in situ tests were complemented by macroscopic tensile and reversible tensile-compression tests to study the Bauschinger effect. In order to reproduce stresses in ferrite and cementite particles, a recently developed micromechanical Internal Length Mean Field (ILMF) model based on a generalized self-consistent scheme is applied. In this designed ferrite–cementite steel, the third "phase" of the model represents finite intermediate "layers" in ferrite due to large geometrically necessary dislocation (GND) densities around cementite particles. The assumed constant thickness of the layers is calibrated thanks to the obtained experimental data. The ILMF model is validated by realistic estimates of the Bauschinger stress and the large difference between mean stresses in ferrite and in cementite phases. This difference cannot be reproduced by classic two-phase homogenization schemes without intermediate GND layers.

1. Introduction

Nowadays, a particular attention is paid in the nuclear industry to the influence of the carbide particle size on material's behavior and local strains and stresses with the aim of better understanding and deriving fracture toughness in the 16MND5 steels used in nuclear reactor vessels [1]. Mean field approaches are often used in designing heterogeneous materials, as they can lead to reasonable estimates of the stress–strain levels in the matrix and in the inclusions, while being very effective in terms of computation costs. The classical mean field homogenization methods used to model the elastic–plastic behavior of heterogeneous materials such as the classic self-consistent models [2,3] or the so-called "β" model [4], can only reproduce particle morphology and volume fraction effects on strain hardening curves. However, they are unable to predict constituent size effects as they do not include any internal length scale in their formulation as discussed in Ref. [5].

Ferrite–cementite steels are two-phase steels which contain cementite hard particles embedded in a ferritic soft matrix. Thus, a high density of collective dislocation arrangements occur near the matrix–particle interfaces in the course of plastic deformation in ferrite. These dislocations were partially considered in Ref. [6] by the presence in the matrix of volume-averaged "geometrically necessary dislocation" (GND) density arising from plastic strain incompatibility between the matrix and particles [7]. More recently, better estimates have been obtained if the saturation of Orowan loop densities is captured at the particle–matrix interfaces [8]. GND densities, a continuous description of lattice incompatibility due to the presence of orderly dislocations, are associated with the development of lattice curvature and long-range internal stresses. In contrast, the stochastic arrangement of "statistically stored dislocations" (SSDs) produce no net Burgers vector and no lattice incompatibility.

Experimentally, layers of dislocations surrounding impenetrable particles have been observed in Refs. [9,10]. Transmission electronic microscopy (TEM) was used to qualitatively understand local dislocation accumulation in the vicinity of ferrite–martensite interfaces in dual-phase steels (DP steels) [11]. However, TEM studies have the shortcoming that only a small area can be observed. Intermediate layers involving large GND densities can also be determined quantitatively by high resolution 2D/3D EBSD measurements as recently done in Ref. [12] in the case of DP steels. However, many statistical data are needed to estimate a mean value of the GND layer thickness due to variations of lattice curvatures as functions of local slip orientations and interface morphologies [12,13].

The present Internal Length Mean Field (ILMF) approach, first introduced in Ref. [14] for Al/SiC alloys, consists in introducing

GND layers of the same finite thickness that surround the impenetrable particles. In addition to particles and matrix, these layers were considered as a third "phase" in the representative volume element (RVE) to describe the collective GND arrangement near the matrix–inclusion interfaces. The thickness of the layer was assumed constant during plastic deformation and was estimated by unit cell Field Dislocation Mechanics (FDM) simulations for Al matrices reinforced by SiC particles [14]. As a result of these full field FDM simulations, the layer thickness was found in the sub-micron range ($\sim$0.3 μm) and was not really dependent on the particle size [14]. Then, this value was introduced in the ILMF approach to capture particle size effects on the overall strain hardening curves [14]. The layer thickness could also be reached by Discrete Dislocation Dynamics (DDD) simulations [15].

The objective of the present paper is first to carry out lattice strain Synchrotron diffraction measurements [16] to deduce the per phase average stresses in cementite and ferrite in addition to the overall stress–strain tensile curves. Second, a "mean value" of the layer thickness introduced in the ILMF approach will be "calibrated" with the experimental per phase average stresses. Indeed, the ratio between the layer thickness and the particle size is expected to have a considerable impact on internal stress self-organization around particles. In addition to the particle size dependent overall strain hardening, it is believed here that reproducing phase stresses altogether with the macroscopic Bauschinger effect for a different alloy composition represents a second and complementary validation of the ILMF approach.

The paper is organized as follows. In Section 2, the two-phase steel constituted of ferrite and cementite is first presented along with its main microstructural features (particle size, volume fraction and morphology). The mechanical tests like simple tension and reversible tension-compression are presented. The macroscopic "Bauschinger stress" is also defined as a function of forward macroscopic strain. After recalling the experimental device for in situ strain analysis during tensile loading with both X-Ray Diffraction (XRD) and ring diffraction techniques in Appendix A, the resulting evolution of lattice strains and stresses in both ferrite and cementite phases during loading are obtained and discussed. In Section 3, the main steps of the ILMF approach are recalled. *A* "3-phase" self-consistent approach with coated particles is designed, which emphasizes the role of large GND densities in the intermediate layers between the particles and the matrix. In this generalized self-consistent scheme, the width of this layer λ is supposed to be constant and is calibrated using the evaluations of mean stresses in both phases provided in Section 2. In Section 4, model predictions in monotonous tension are analyzed in comparison with experimental results. The importance of the layer thickness and the contribution of GNDs to isotropic hardening by dislocation tangles are evidenced in terms of the high experimental difference found between both stresses in ferrite and cementite. The impact of the particle aspect ratio is also discussed in Section 4. A part of the Bauschinger stress is then estimated and discussed from the stresses in both phases obtained at the end of the tensile stage.

2. Experimental

2.1. Material and mechanical tests

The studied material is a two-phase steel which contains 0.4 wt% C and 0.7 wt% Mn. It is constituted of ferritic grains with average size of 15 μm and with small cementite (Fe_3C) particles as shown in Fig. 1. The processing of this steel was constituted of a first heat treatment at 900 °C for 5 min followed by quenching. Then, the obtained martensitic state was tempered at high temperature (690 °C) for 60 h to obtain the designed ferrite–cementite steel. The resulting microstructure was observed with a JEOL 7001F SEM-FEG. The resulting Fe_3C carbides are both located in inter- and intra-granular regions (Fig. 1a). Most of particles are located inside grains although larger particles were observed at grain boundaries. No strong clustering of particles was observed and their volume fraction is 5.7%. This value was determined by neutron diffraction technique. The spatial size distribution of particles in the ferrite matrix is displayed in Fig. 1b. This distribution is approximately log-normal with an average particle size of 0.73 μm. As shown in Fig. 2, the cumulated frequency of the particle shape factor of particles obtained by image analysis shows that the aspect ratio of carbides varies essentially between 1 and 2 with an average value of 1.5. It is noteworthy that no specific orientation distribution was observed regarding the particle morphology. The effect of particle aspect ratio will be discussed in Section 4.

Constant low strain rate tension and reversible tension–compression tests were performed at room temperature. Flat specimens with 5 mm by 1 mm rectangular cross sections were

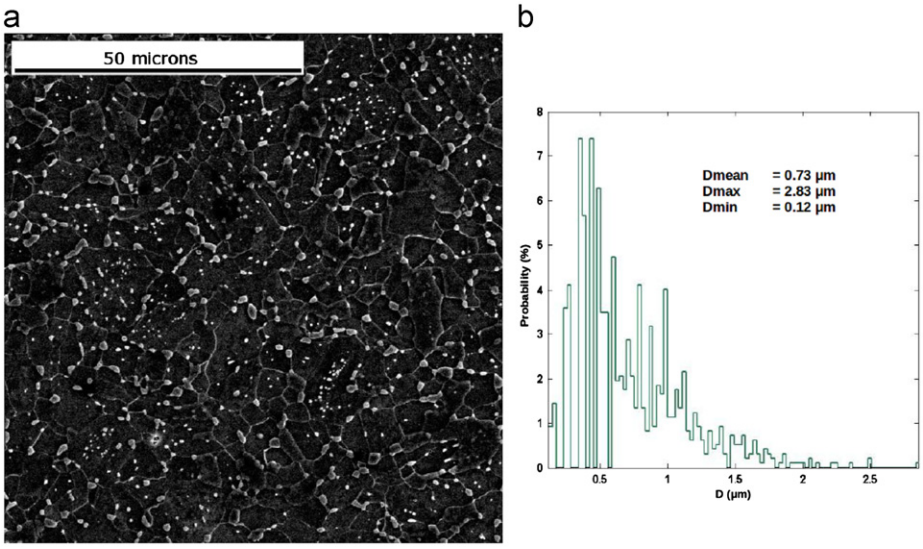

Fig. 1. (a) SEM image of the designed ferrite-Fe_3C carbides steel with particle spatial distribution, (b) probability distribution of measured particle size *D*.

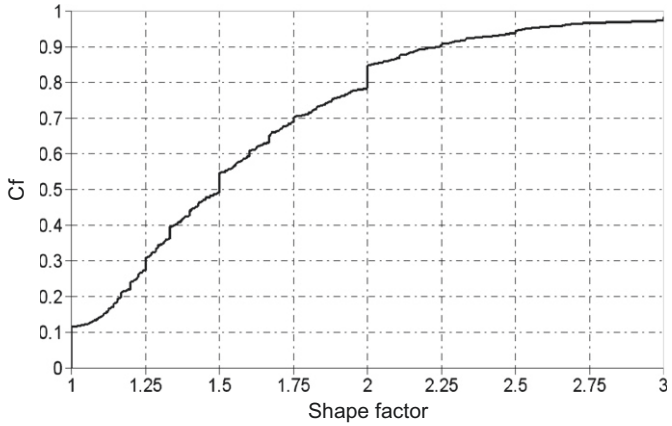

Fig. 2. Cumulated frequency (C_f) as a function of particle shape factor in the as-received designed steel.

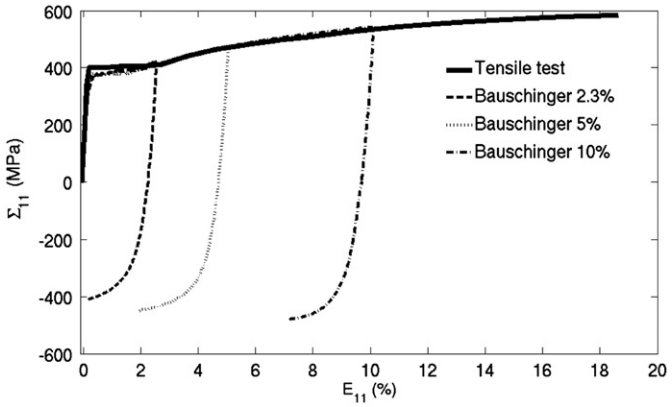

Fig. 3. Tensile and tension–compression tests at room temperature with quasi-static applied strain rate.

used. The gauge length was 24 mm and the applied strain rate was $10^{-4}\,s^{-1}$. Fig. 3 gathers all results regarding monotonous and reverse loadings. In addition to the monotonous tension up to 18% of strain, three Bauschinger tests were performed after 2.3%, 4.9% and 10% of forward tensile strain. A remarkable Bauschinger effect was observed and reflects the presence of significant internal stresses. A measure of the Bauschinger effect can be provided by the so-called "Bauschinger stress" denoted X and defined as $X=(\Sigma^{(1)}+\Sigma^{(2)})/2$ where $\Sigma^{(1)}$ and $\Sigma^{(2)}$ are respectively the forward macroscopic flow stress at the end of the tension stage and the reverse macroscopic yield stress in the compression stage. Let us note that this definition of X is half the quantity defined in Ref. [17]. Fig. 4 reports the measured macroscopic Bauschinger stress X as a function of macroscopic forward tensile strain. A saturation of X with increasing tensile strain is observed. Furthermore, the high values obtained for X suggest that the self-organization of GNDs around cementite particles increase internal stresses. Thus, a significant intra-phase kinematic hardening is expected in addition to that due to the mechanical interactions between ferritic grains only. This trend will be discussed in the light of the stresses in both phases deduced from experiments and from the micromechanical model in Section 4.

2.2. Results of diffraction analyses

2.2.1. XRD measurements for stress evolution in ferrite

The XRD experimental device and the stress analyses are respectively presented in Sections A.1 and A.2 of Appendix A. Stress analyses obtained from the XRD measurements show that

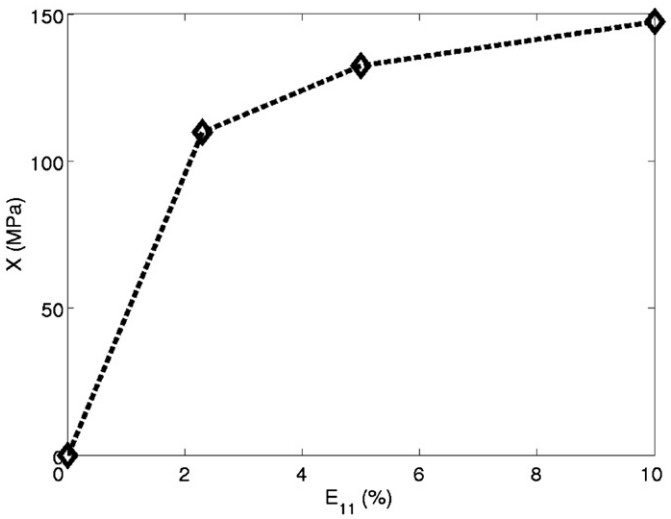

Fig. 4. Measured Bauschinger stress X (the definition is given in the text) as a function of forward tensile strain at room temperature with quasi-static applied strain rate.

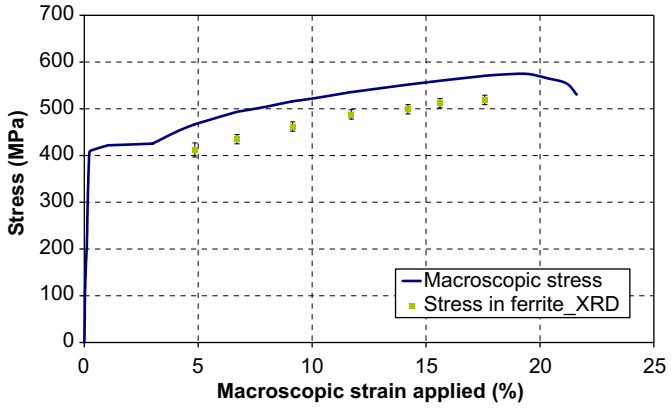

Fig. 5. Evolution of the average stress in ferrite during loading (XRD measurements). The error bars for stress uncertainties in ferrite are provided (see text for values).

ferrite acts as the soft phase in the steel with a level of stress lower than the macroscopic stress (Fig. 5). The observed difference between the macroscopic stress and the average stress in ferrite increases with the applied strain without exceeding 100 MPa. It is maximum before failure for a stress in ferrite around 520 MPa. This difference is quite the same as the one obtained in ferrite of a pearlitic steel using neutron diffraction [18]. Conversely, stresses in cementite should be very high during tensile loading. It is useful to know the order of magnitude of the maximum stress reached in this phase. Since the XRD method does not provide directly the uniaxial stress in cementite along the tensile direction (x_1) denoted $\sigma_{11}^{Fe_3C}$, this one can be estimated using a simple mixture rule as follows:

$$\Sigma_{11}=f_{Fe\alpha}\sigma_{11}^{Fe\alpha}+f_{Fe_3C}\sigma_{11}^{Fe_3C} \quad (1)$$

where Σ_{11} is the macroscopic tensile stress, $\sigma_{11}^{Fe\alpha}$ is the uniaxial stress in ferrite during loading determined by XRD, $f_{Fe\alpha}$ and f_{Fe_3C} are respectively the volume fraction of ferrite and cementite in the steel. The results are presented in Table 1 with an uncertainty of ± 10 MPa for the stress in ferrite and ± 170 MPa for the stress in cementite. These results show that the stress in cementite can reach values around 1500 MPa at 18% of macroscopic strain before failure.

Table 1
Stress values obtained in ferrite and cementite during tensile loading using a simple mixture rule (Eq. (1)). Values are given with an uncertainty of ± 10 MPa in ferrite and ± 170 MPa in cementite.

Macroscopic strain (%)	Stress in ferrite (MPa) XRD measurements	Stress in cementite (MPa) mixture rule
0	0	0
4.85	410	1375
6.7	435	1470
9.15	460	1410
11.7	490	1330
14.2	500	1430
15.6	510	1355
17.55	520	1430

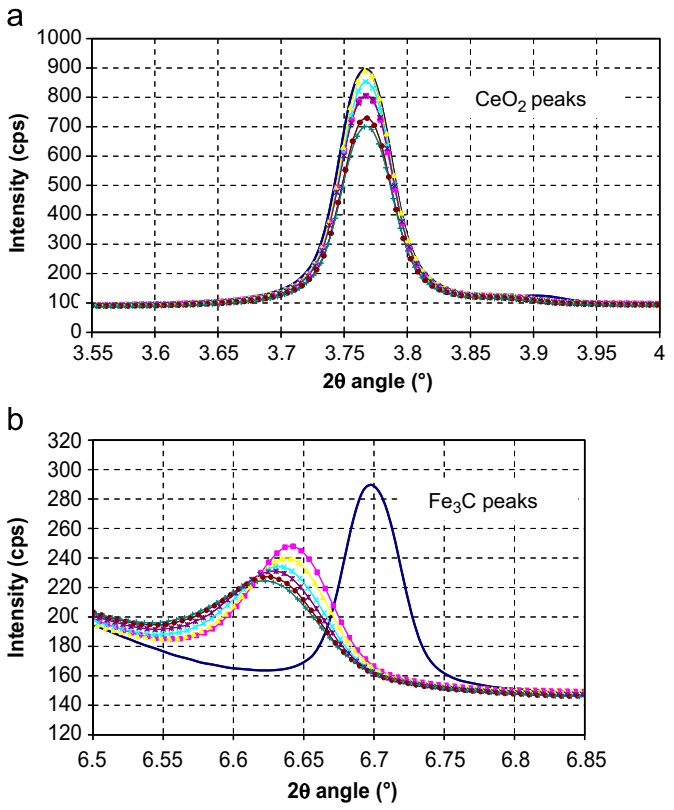

Fig. 6. Position of the diffraction peaks during loading: (a) CeO_2 peaks always at the same 2θ angle, (b) Cementite peaks gradually shifted to smaller 2θ angles (ε_{11} strain).

2.2.2. *Synchrotron ring diffraction analyses for elastic strain evolutions*

In situ tensile tests were performed at the European Synchrotron Radiation Facility (ESRF), using the ID11 beamline with high energy X-rays. The stress analyses in cementite are possible using ring diffraction measurements detailed in Appendix A. During loading, the CeO_2 calibrant (see Section A.1 of Appendix A) is crucial for the calculation of the elastic strains from the different rings. The different peaks of CeO_2 must remain at the same 2θ position whereas the peaks of ferrite and cementite are shifting. It is thus possible to see the gradual shift of these peaks with increasing applied macroscopic strain (Fig. 6). Considering the two masks defined in Section A.1 of Appendix A, the rings integration leads to the evolution of ε^e_{11} and ε^e_{22} elastic strains vs. macroscopic applied strain for both ferrite and cementite phases (see Section A.2 in Appendix A). These elastic strains are reported in Fig. 7. The uncertainties on strains are 5×10^{-5} for ferrite and 2×10^{-4} for cementite. As expected, since the (x_1) direction is the tensile direction, the values for ε^e_{11} and ε^e_{22} are respectively positive and negative. Moreover, the level of elastic strain in cementite is about five times higher than in the ferrite in the plastic range. This can be explained by the difference in mechanical properties between both phases and particularly their yield stress. As soon as the macroscopic initial yield point is reached for this steel, ferrite undergoes plastic deformation in contrast with cementite particles which are supposed to remain elastic. The obtained curve for elastic strain in cementite as a function of the macroscopic strain shown in Fig. 7 is not linear, especially in the plastic range. This is due to elastic–plastic strain accommodation between ferrite and cementite during plastic flow in ferrite. The stress values in the tensile direction are then estimated in each phase using linear elastic formulation with the hypothesis $\varepsilon^e_{22}=\varepsilon^e_{33}$ as follows:

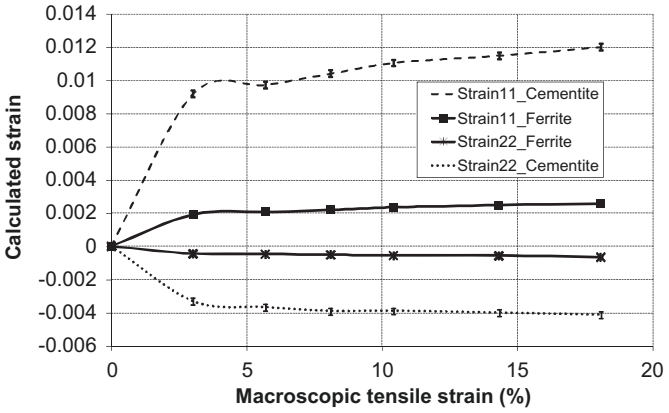

Fig. 7. Evolution of elastic strains ε^e_{11} and ε^e_{22} for both ferrite and cementite phases during loading: synchrotron measurements. The error bars for elastic strain uncertainties are provided (see text for values).

$$\sigma_{11}=\frac{E}{1+\nu}\varepsilon^e_{11}+\frac{E\nu}{(1+\nu)(1-2\nu)}\left(\varepsilon^e_{11}+2\varepsilon^e_{22}\right) \quad (2)$$

where E and ν are respectively the Young's modulus and Poisson ratio of each phase considering the {110} planes for ferrite and the {122} planes for cementite. The main difficulty is to determine E and ν in Eq. (2) for each considered planes family. Therefore, an inverse method is proposed in the following way. First, E and ν are identified for the {110} planes in ferrite so that the σ_{11} stress in this phase is consistent with the stress values obtained using XRD: $E^{Fe_\alpha}_{\{110\}}=200\pm1$ GPa and $\nu=0.29$. These values are consistent with those reported in Refs. [19,20]. $E^{Fe_\alpha}_{\{110\}}$ is close to the calculated Young's modulus of 225 MPa in bcc iron single crystal by considering the three elastic constants $C_{11}=237$ GPa, $C_{12}=134$ GPa and $C_{44}=116$ GPa. Then, since the σ_{11} stress in cementite is unknown, E and ν are identified for the {122} planes in this phase by the values $E^{Fe_3C}_{\{122\}}=160\pm3$ GPa and $\nu=0.33$. These values are obtained from the macroscopic stress which is calculated with a mixture rule similarly to that used in Eq. (1) and must fit the macroscopic stress given by the tensile micromachine. The obtained value for $E^{Fe_3C}_{\{122\}}$ is similar to that determined for the same cementite planes family in Ref. [20] using synchrotron radiation. In this case, the maximum stress that cementite can bear is almost 2000 MPa as reported in Fig. 8. This value is a little bit higher than that estimated from XRD analyses using a mixture rule, but is certainly more accurate because this is determined from direct elastic strain measurements in cementite. Even if a linear elastic formulation was considered for the calculation, the order of magnitude of the maximum stress in cementite is found to be realistic.

3. Internal length mean field (ILMF) model

3.1. Constitutive equations with GND layers around particles

In this section, a small strain incremental Internal Length Mean Field (ILMF) model for elastic–plastic heterogeneous materials [14] is applied to the designed ferrite–cementite steel. Ferrite is considered elastic–plastic with a statistically homogeneous distribution of purely elastic cementite particles with average diameter D as described in Fig. 9. Since the average particle size D is much smaller than the average grain size, the polycrystalline aspect will be disregarded. In the following, three "phases" are considered. The first phase is the matrix phase representing ferrite far away from the particles (denoted M). This phase plastically deforms and hardens only through the evolution of a SSD density ρ^M_{SSD}. The second phase represents cementite particles (denoted C) which are supposed elastic and of same ellipsoidal shape. Let us denote the respective matrix and particle volume fractions by f_M and f_C. In order to improve the capability of mean field approaches, the physical accumulation of excess dislocations at the matrix–inclusion interfaces is here taken into account by introducing a third "phase" (L) with volume fraction f_L. This one consists in intermediate layers of same finite thickness λ containing a large GND density and surrounding the particles (Fig. 9). λ provides the internal length of the model and is assumed to be constant during deformation. The layers and the particles form composite inclusions ($L+C$) with same axis ratios (homothetic topology). Thus, the "layer phase" volume fraction f_L is given by $f_L=f_C((a+\lambda)(b+\lambda)(c+\lambda)-R^3)/R^3$ where a, b and c are respectively the semi-axes of the ellipsoidal particles in the x_1, x_2 and x_3 directions associated with the macroscopic principal stress directions. Hence, the average radius $R=D/2$ of the volume equivalent spherical particles is defined such as $abc=R^3$. The Representative Volume Element (RVE) is shown in Fig. 9. The particles are supposed to deform elastically such as $\dot\sigma^C_{ij}=c^C_{ijkl}\dot\varepsilon^C_{kl}$ where c^C_{ijkl} are the linear elastic moduli of cementite particles. A $J2$ plastic flow theory is assumed for the hardening of the matrix and the layer. The consistency condition for plastic flow writes for each phase K ($K=M, L$)

$$\dot\sigma^K_{eq}=\dot\sigma^K_{ref} \tag{3}$$

where $\sigma^K_{eq}=(3/2s^K_{ij}s^K_{ij})^{1/2}$ is the equivalent Von Mises stress in phase K, s^K_{ij} are the deviatoric stresses and σ^K_{ref} describes the evolution of isotropic hardening. In the layer phase L, the latter follows the evolution of the sessile SSD density given by a Kocks–Mecking law [21] modified to account for interactions with the GNDs

$$\dot\sigma^L_{ref}=\frac{M\alpha\mu b}{2\sqrt{\rho^L_{SSD}}}\dot\rho^L_{SSD}=\frac{M^2\alpha\mu b}{2\sqrt{\rho^L_{SSD}}}\left(\frac{k}{b}\sqrt{\rho^L_{SSD}}-f\rho^L_{SSD}+k_{GND}\rho^L_{GND}\right)\dot\varepsilon^{pL}_{eq}=H_L\dot\varepsilon^{pL}_{eq} \tag{4}$$

where M is the Taylor factor. For each K, $\dot\varepsilon^{pK}_{eq}$ is the von Mises equivalent plastic strain rate $\dot\varepsilon^{pK}_{eq}=\left(2/3\dot\varepsilon^{pK}_{ij}\dot\varepsilon^{pK}_{ij}\right)^{1/2}$ and H_K denotes the incremental isotropic hardening modulus. The variables ρ^L_{SSD} and ρ^L_{GND} are respectively the SSD and GND densities in the layer phase. The additional term $k_{GND}\rho^L_{GND}$ accounts for the contribution of the GNDs to forest dislocation hardening through dislocation tangles [22]. The "classic" Kocks–Mecking law [21] without this term is used for (M) as only SSD densities are present in the matrix

$$\dot\sigma^M_{ref}=\frac{M\alpha\mu b}{2\sqrt{\rho^M_{SSD}}}\dot\rho^M_{SSD}=\frac{M^2\alpha\mu b}{2\sqrt{\rho^M_{SSD}}}\left(\frac{k}{b}\sqrt{\rho^M_{SSD}}-f\rho^M_{SSD}\right)\dot\varepsilon^{pM}_{eq}=H_M\dot\varepsilon^{pM}_{eq} \tag{5}$$

The scalar GND density evolution in the layer phase $\dot\rho^L_{GND}$ is derived from simplifications of the transport equation of GNDs for a spherical elastic inclusion in spherical coordinates. Even though the elastic distortion may gradually vary from the matrix–particle interfaces (see e.g. Ref. [14]), the (average) scalar GND density evolution in the layer phase L of the ILMF scheme can be reasonably approximated by

$$\dot\rho^L_{GND}\approx\frac{\dot\varepsilon^{pM}_{eq}}{\lambda b} \tag{6}$$

Eq. (6) clearly implies a strong influence of the layer thickness λ on the GND density inside the layer and therefore on the overall strain hardening. The local consistent tangent elastic–plastic

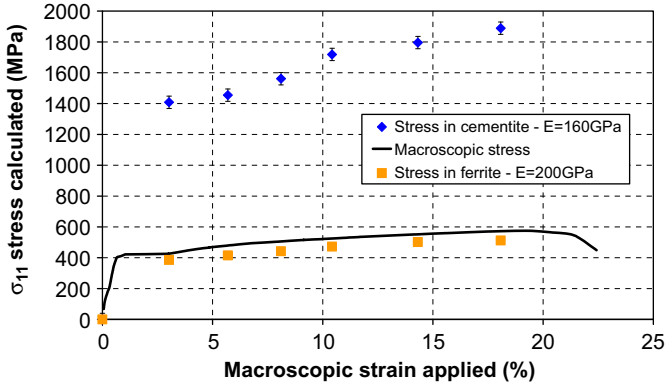

Fig. 8. Evolution of the σ_{11} stress for both ferrite and cementite phases during loading. $E^{Fe_\alpha}_{\{110\}}=200\pm1$ GPa and $E^{Fe_3C}_{\{122\}}=160\pm3$ GPa. The error bars for stress uncertainties in cementite are provided (see text for values).

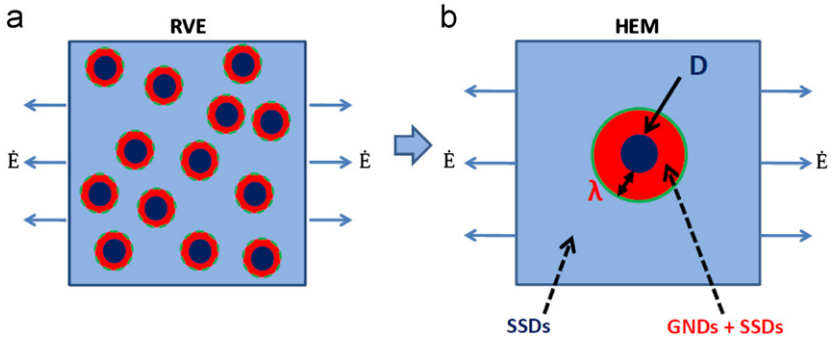

Fig. 9. (a) Representative volume element of the ferrite/cementite system (polycrystalline aspects and grain boundaries are disregarded) with GND layers constrained as a finite "interphase" of constant thickness λ between the ferrite matrix (denoted M in the text) and the cementite particles (denoted C in the text). Note that the morphology of the coated inclusions can be ellipsoidal but the topology remains homothetic. (b) The problem is solved using a Homogeneous Equivalent Medium (HEM) with effective elastic-properties determined by the Self-Consistent scheme.

moduli l^K_{ijkl} relating the stress rate and the total strain rate in each phase K (with $K=M, L$) can be computed as

$$\dot{\sigma}^K_{ij} = l^K_{ijkl}\,\dot{\varepsilon}^K_{kl} \tag{7}$$

Here, an "isotropization" of these moduli is applied because usual anisotropic moduli are known to overestimate the global and local stresses [23–25]. It was checked in the case of a two-phase material (matrix and inclusions) with high contrast between both phases [23] that "isotropized" moduli lead to results fairly close to finite element results. In their "isotropized" form, the tangent moduli write $l^K_{ijkl} = 3K_K J_{ijkl} + 2\varphi_K K_{ijkl}$, where for each phase K, K_K is the bulk elastic modulus and $\varphi_K = (\mu_K H_K)/(3\mu_K + H_K)$ contains both the shear modulus μ_K and the hardening modulus H_K (present in Eq. (4) and Eq. (5)). The 4th order tensors $J_{ijkl} = (1/3)\delta_{ij}\delta_{kl}$ and $K_{ijkl} = 1/2(\delta_{ik}\delta_{jl} + \delta_{il}\delta_{jk} - (2/3)\delta_{ij}\delta_{kl})$ are respectively hydrostatic and deviatoric orthogonal projection tensors.

3.2. Homogenization strategy

Homogenization for this kind of topology is often performed through a generalized self-consistent scheme introduced by Christensen and Lo [26] and extended by Hervé and Zaoui [27,28], Marcadon et al. [29] for elastic composites with spherical multi-coated inclusions. Cherkaoui et al. [30] solved the case of heterogeneous elastic composites with more general ellipsoidal coated inclusions. The case of general ellipsoidal multi-coated inclusions for elastic composites with eigenstrains was recently solved by Berbenni and Cherkaoui [31]. Here, the procedure follows the one investigated in Refs. [30,31] using the Hill's interfacial operators [32] and is adapted to elastic–plastic heterogeneous materials with "isotropized" tangent moduli as introduced in Section 3.1. The material is supposed to be constituted of "3 phases". As described in Fig. 9, the RVE is subjected to macroscopic strain rates $\dot{E}_{ij}$. By denoting the effective tangent moduli l^{eff}_{ijkl} for the Homogeneous Equivalent Medium (HEM in Fig. 9), the macroscopic stress rates $\dot{\Sigma}_{ij}$ is related to $\dot{E}_{ij}$ as follows:

$$\dot{\Sigma}_{ij} = l^{eff}_{ijkl}\dot{E}_{kl} \tag{8}$$

The imposed strain rates $\dot{E}_{ij}$ are the volume averages of the strain rates in the three phases, and the macroscopic stress rates $\dot{\Sigma}_{ij}$ are the volume averages of stress rates in the three phases as follows:

$$\begin{aligned}\dot{E}_{ij} &= f_C\dot{\varepsilon}^C_{ij} + f_L\dot{\varepsilon}^L_{ij} + f_M\dot{\varepsilon}^M_{ij}\\ \dot{\Sigma}_{ij} &= f_C\dot{\sigma}^C_{ij} + f_L\dot{\sigma}^L_{ij} + f_M\dot{\sigma}^M_{ij}\end{aligned} \tag{9}$$

Let us now write the strain rate concentration equations as follows:

$$\begin{aligned}\dot{\varepsilon}^C_{ij} &= A^C_{ijkl}\dot{E}_{kl}\\ \dot{\varepsilon}^L_{ij} &= A^L_{ijkl}\dot{E}_{kl}\end{aligned} \tag{10}$$

where A^C_{ijkl}, A^L_{ijkl} are respectively the strain rate concentration tensors for phases C and L. They are determined by using the interfacial operator technique (see the appendix in Ref. [14] for details). The strain rates in the matrix phase $\dot{\varepsilon}^M_{ij}$ can easily be obtained from Eqs. (9) and (10), and the corresponding stress rates $\dot{\sigma}^M_{ij}$ follow from Eq. (7). Furthermore, Eqs. (8–10) give

$$l^{eff}_{ijkl} = l^M_{ijkl} + f_C\left(c^C_{ijmn} - l^M_{ijmn}\right)A^C_{mnkl} + f_L\left(l^L_{ijmn} - l^M_{ijmn}\right)A^L_{mnkl} \tag{11}$$

The effective tangent moduli l^{eff}_{ijkl} require the calculation of the strain rate concentration tensors in Eq. (10). This is performed by the self-consistent method where homothetic ellipsoidal particles and layers are embedded in the HEM (Fig. 9). In this description, the HEM contains C, L and M. The strain rate concentration tensors simplify into [14]

$$A^C_{ijkl} = \left[\begin{array}{l} I_{ijkl} + T^{eff}_{ijmn}\left(c^C_{mnkl} - l^{eff}_{mnkl}\right) - \\ \frac{f_L}{f_C+f_L}\left[T^{eff}_{ijmn}\left(l^L_{mnpq} - l^{eff}_{mnpq}\right)T^L_{pqrs} - \left(T^{eff}_{ijrs} - T^L_{ijrs}\right)\right]\left(l^L_{rskl} - c^C_{rskl}\right)\end{array}\right]^{-1} \tag{12}$$

and

$$A^L_{ijkl} = [I_{ijpq} - T^L_{ijmn}\left(l^L_{mnpq} - c^C_{mnpq}\right)]A^C_{pqkl} \tag{13}$$

where the 4th order symmetric tensors T^{eff}_{ijkl} (resp. T^L_{ijkl}) are derived from the classic symmetric Eshelby tensors associated with l^{eff}_{ijkl} (resp. l^L_{ijkl}) and, I_{ijkl} is the 4th order unit tensor.

4. Model calibration and validation

4.1. Key physical parameters

The parameter identification was performed using simple macroscopic tensile response as well as the ferrite and cementite stresses reported in Fig. 8 directly estimated from lattice strain measurements in Section 2.2. The average inclusion diameter (assuming equivalent spherical shape) is taken as $D=0.73$ μm and the volume fraction of cementite particles (Fe_3C) is $f_C=5.7\%$. The elasticity constants are supposed linear isotropic and the Young's modulus for ferrite (matrix phase and layer) is classically $E^{Fe\alpha}=210$ GPa. Young's modulus for cementite (C) is taken equal to $E^{Fe3C}=230$ GPa following recent estimated isotropic elastic constants for cementite [33]. The Poisson ratio is supposed uniform (see Table 2). Isotropic strain hardening parameters k and f for ferrite were adjusted around typical values recently identified for purely ferritic steels (no cementite particles) with different grain sizes [34]. These parameters were adjusted to reproduce the saturation of experimental macroscopic strain hardening with strain. The initial SSD densities in the matrix and the layers are $10^{10}\ m^{-2}$. The initial GND density in the layer is $10^{10}\ m^{-2}$. The initial critical stresses in the matrix and the layer are 100 MPa. All other parameters are listed in Table 2.

As anticipated in Section 1, the key parameter is the layer thickness λ. Here, its value is calibrated in order to reproduce the elastic strain measurements and corresponding stresses in both metallurgical phases (Fig. 8). In order to compare the model predictions to the experimental values obtained for the tensile stress in ferrite, the latter is computed as a function of the average stress in the matrix (M) and the layer (L) phases

$$\sigma^{Fe\alpha}_{11} = (f_M\sigma^M_{11} + f_L\sigma^L_{11})/(f_M + f_L) \tag{14}$$

Fig. 10 shows the reference model predictions for the macroscopic and phase stress curves during simple tension in the (x_1) direction with elongated ellipsoidal particles aligned in the tensile direction with a constant aspect ratio of 1.5. The latter corresponds to the averaged value for aspect ratio of particles given in Fig. 2. While fitting the experimental macroscopic strain

Table 2
List of material parameters used in the model to fit both experimental macroscopic and local stress curves given in Fig. 10. For the simulation, the particles are ellipsoidal inclusions aligned in the tensile direction and with a constant aspect ratio of 1.5. The GND layers around particles have constant thickness λ (0.3 μm).

α	M	λ (μm)	$E^{Fe\alpha}$ (GPa)	E^{Fe3C} (GPa)
0.4	3	0.3	210	230
$\nu_{Fe\alpha}$	ν_{Fe3C}	k	f	b (Feα) (m)
0.29	0.29	0.03	14	2.5×10^{-10}

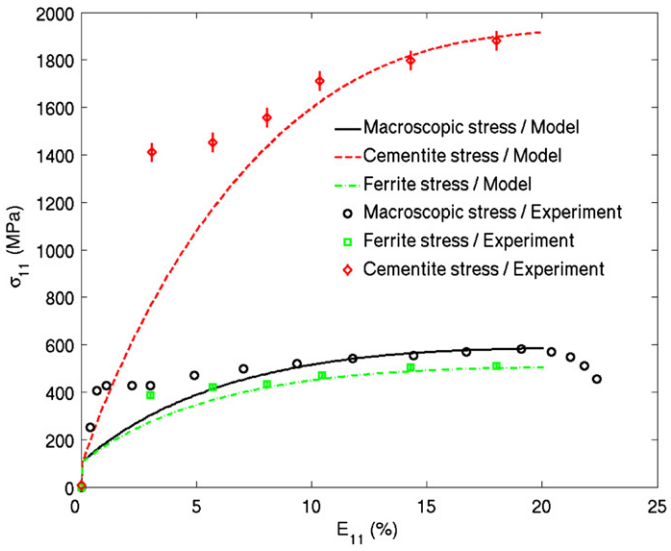

Fig. 10. Macroscopic and phase stresses predicted by the model with an aspect ratio of 1.5 for ellipsoidal particles aligned in the tensile direction. Experimental estimations of Fig. 8 are superimposed for comparison.

hardening curve, λ is adjusted to capture the significant experimental difference between the tensile stresses in ferrite and cementite. Concurrently, the value of k_{gnd} was also calibrated and taken to be 250 k, a value 2.5 higher than that used in Ref. [14]. After the yield stress, the discrepancy between model stress response and experimental data up to 5% of overall strain is clearly due to a Lüders plateau which originates from a macroscopic plastic instability seen for this steel in tension. The micromechanical ILMF model is based on a homogenization scheme which does not aim to account for strain localization phenomena like macroscopic Lüders bands. In the present constitutive framework, the first perfect plastic behavior after the initial yield point is not described and the study is only focused on the influence of GND layers on the homogeneous strain hardening behavior after a few percents of overall strains (see Fig. 10).

Thus, a sub-micron value of 0.3 μm was found to give a reasonable fit to experimental results in Fig. 10 at overall strains larger than 5%. It is noteworthy that a layer thickness on the order of 0.3 μm was also estimated by Field Dislocation Mechanics (FDM) simulations in the framework of Al matrices reinforced by SiC particles [14] even though particle sizes were different from the present study. In Ref. [14], that allowed capturing particle size effects on overall strain hardening for two Al matrix compositions with the ILMF model. Here, the present calibration of the ILMF model using combined XRD and Synchrotron diffraction measurements gives same order of magnitude for λ. Let us note that the particle sizes were larger in Ref. [14] than in the present designed ferrite–cementite steel. From these results and with a simple reasoning using Eq. (6) which is a simplification of the GND transport equation, it seems that the layer thickness λ is especially influenced in our approach by the ratio between accumulated plastic strain in the matrix phase and the uniform GND density in layers around particles. Thus, the formulation does not give a direct influence of particle size. In this sense the model is different from classic models [6,7] which considered an average scalar GND density in the overall matrix but did not consider spatial GND distributions in finite layers around particles and characterized by an internal length λ. Accordingly, it is not unrealistic to find same order of magnitude for GND layer thickness even though the microstructural systems may have different particle size.

In the present study, a significant difference of about 1300 MPa at the end of forward straining is obtained between the tensile stresses in ferrite and in cementite in good agreement with experimental estimations. The layer thickness λ, which is about half the particle size, and the GND contribution to isotropic hardening (through k_{gnd}) are responsible for such a difference. This difference results from a higher stress in the layer than in the matrix because of the physical GND contribution to isotropic hardening (Eq. (4)). We also checked that such difference was not reachable with classic two-phase homogenization schemes for which $\lambda \to 0$ ($f_L \to 0$) using elastic–plastic "isotropized" tangent moduli even if these formulations were calibrated by classic finite element cell calculations [23,24]. As evidenced in Fig. 11, when the layer thickness is divided by a factor of ten while keeping unchanged the value of k_{gnd}, the difference between both phase stresses is much smaller (about 400 MPa). This difference is also reduced when $k_{gnd}=0$ while keeping the layer thickness (about 300 MPa) unchanged. It was checked that the huge experimental difference between the stresses in ferrite and in cementite cannot be captured by the model with a too small layer and/or a too small value of k_{gnd}, even by using new identified physical strain hardening parameters. These results show the impact on the induced length scale parameter λ on local stress estimates using "isotropized" tangent moduli.

Concurrently with the effect of the GND layer thickness λ, the aspect ratio of particles is also a parameter which can affect significantly the difference between phase stresses. As shown in Fig. 11, when the aspect ratio is increased up to 2 with ellipsoidal particles aligned in the tensile direction, the difference increases. Conversely, when an aspect ratio of 1.5 is taken into account with ellipsoidal particles aligned in the normal direction to tensile loading (i.e. the transverse direction), the difference is significantly reduced. A stress difference reduction was also found when particles are assumed spherical. Thus, the model predictions suggest that ellipsoidal particles with same average aspect ratio of 1.5 aligned in the tensile direction carry more loads and contribute to increase the difference between the stresses in ferrite and cementite, as compared to spherical particles for the same calibrated GND layer thickness λ. However, it should be

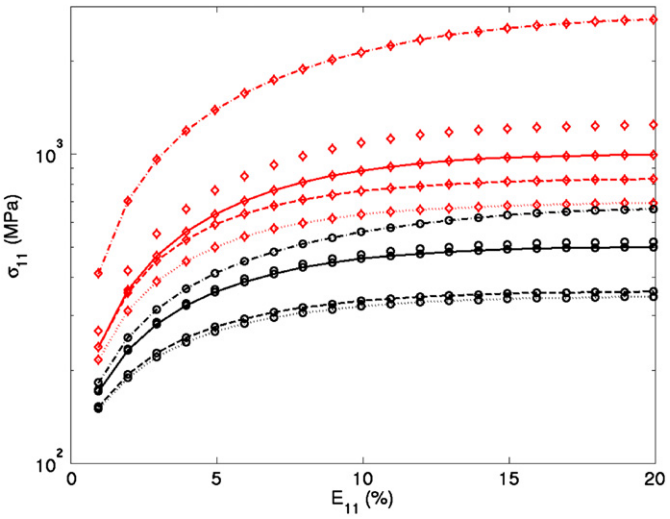

Fig. 11. Evolution of the model predictions when: the layer thickness λ is divided by a factor of 10 with respect to its value in Table 2, i.e. $\lambda=0.03$ μm (dashed lines), $k_{gnd}=0$ (dotted lines), an aspect ratio of 2 is accounted for in the tensile direction (mixed lines), an aspect ratio of 1.5 is considered normal to the tensile direction (full lines), and, particles are assumed spherical (no lines). The circles and diamonds denote the macroscopic stress and the stress in cementite particles, respectively.

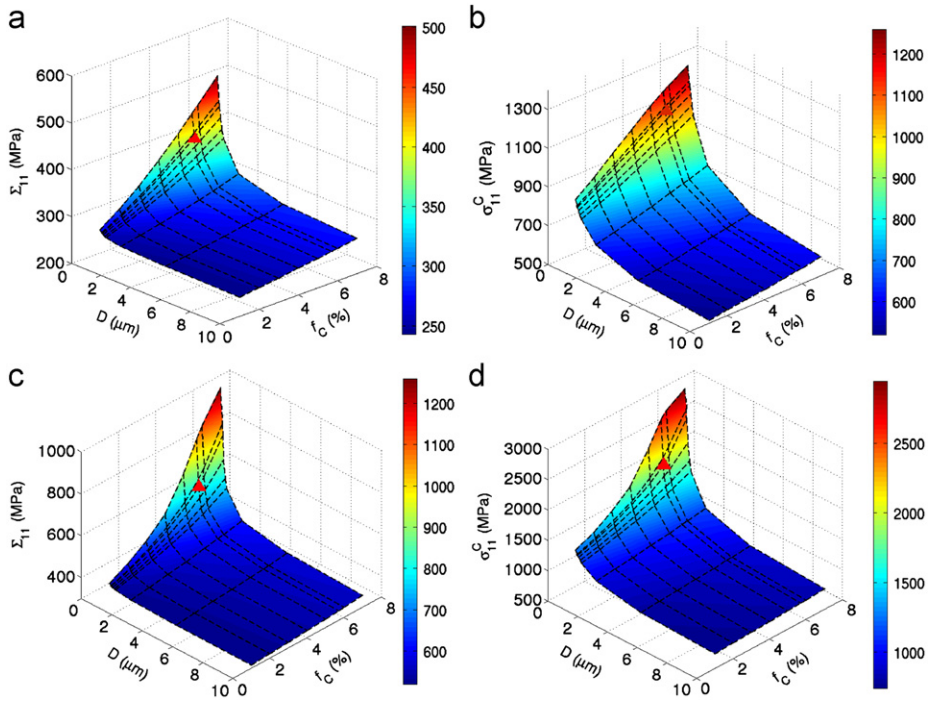

Fig. 12. ILMF model predictions with materials parameters given in Table 2 of macroscopic tensile stresses Σ_{11} at 5% of strain (a), 20% of strain (c) and particle tensile stresses σ^C_{11} at 5% of strain (b), 20% of strain (d). The values are reported as functions of f_C (particle volume fraction) and D (equivalent average particle size diameter). The triangles indicate the predicted values for the ferrite-cementite steel studied in the present paper.

noted that no preferential orientation of particles with respect to tensile direction was observed (Fig. 1). The ILMF model might be extended to account for particle orientation distribution but this is left for future study.

For the material parameters given in Table 2, the influence of particle volume fraction f_C and diameter D is investigated. Fig. 12 shows the maps of macroscopic tensile stress Σ_{11} and particle tensile stress σ^C_{11} as functions of f_C and D. These maps are given at 5% (resp. Fig. 12a and b) and at 20% (resp. Fig. 12c and d) macroscopic strains. The stress levels and the aforementioned difference between both phase stresses increase with increasing f_C. A "smaller is harder" size effect of the particle diameter D is obtained due to a GND layer thickness of 0.3 μm. Remarkable size effects can be obtained when D is in the order of λ. Conversely, size effects become gradually negligible when D reaches values, which are much larger than λ. In Fig. 12, we limit the values of D and f_C such that the GND layer volume fraction f_L does not exceed 50%. This limit guaranties that the assumption of uniform stress/strain fields in the GND layers remains reasonable and also that neighboring GND layers do not overlap, which would make the model incorrect. The largest value of f_L is about 50% for a particle diameter of 0.6 μm and a particle volume fraction of 7%. In this case, it was checked that the average particle spacing L, given by $L=(\pi D^2/(4f_C))^{1/2}$ [6], is about 2 μm. As the GND layer thickness is 0.3 μm, there is no overlap of GND layers in a statistical average sense. For the smallest particle diameter ($D=0.6$ μm) and largest particle volume fractions ($f_C=7\%$), the difference between phase stresses is important and the tensile stresses in the particles become very high ($\sim$2500 MPa at 20% of macroscopic strain). In each subfigure of Fig. 12, the triangles indicate the predicted values for the particular case of the designed ferrite–cementite steel studied in the present paper for which $\lambda/D\approx 0.4$. It was then checked that for a GND layer thickness divided by a factor ten ($\lambda=0.03$ μm), almost no size effect occurs in the present range of particle volume fractions and sizes. Same size independent results are obtained if the contribution of GNDs to isotropic hardening is cut off ($k_{gnd}=0$) with $\lambda=0.3$ μm.

4.2. Bauschinger stress

In order to validate the order of magnitude found for the layer thickness λ (0.3 μm) in Section 4.1, an estimate of the Bauschinger stress from the results of the ILMF model is now developed. During complex loadings like Bauschinger tests performed in Section 2.1, the GND density content may evolve in complex ways due to the annihilation of dipolar structures in the transient regime between the direct and reverse loading paths as recently observed by FDM simulations [35,36]. Thus, the evolution of GND density in the layer phase is probably more complex than Eq. (6) which is only valid for monotonic loading. It would require new understanding using either DDD or FDM simulations to extend the present GND backstress formulation to strain path changes. For this reason, the ILMF approach is limited to the prediction of monotonic responses for this steel. Usually, in order to highlight the resulting macroscopic backstress originating here from "inter-phase" stresses (i.e. the so-called Bauschinger stress) the predictions of reversible responses are needed.

However, a simple efficient way to estimate at least one part of the overall experimental Bauschinger stress X reported in Fig. 4 is to assume the steel as a two-phase composite material. Accordingly, we can derive an estimate of the Bauschinger stress now denoted X' from the phase stresses in both ferrite and cementite after monotonic tensile loadings, as previously reported with both experimental and ILMF model results (Fig. 10). The analysis consists in considering the uniaxial stresses at the end of the tensile stage and applying the following formula to estimate X'.

$$X' = f_C\left(\sigma_{11}^{Fe_3C}-\Sigma_{11}\right) = -(1-f_C)\left(\sigma_{11}^{Fe\alpha}-\Sigma_{11}\right) = f_C(1-f_C)\left(\sigma_{11}^{Fe_3C}-\sigma_{11}^{Fe\alpha}\right) \tag{15}$$

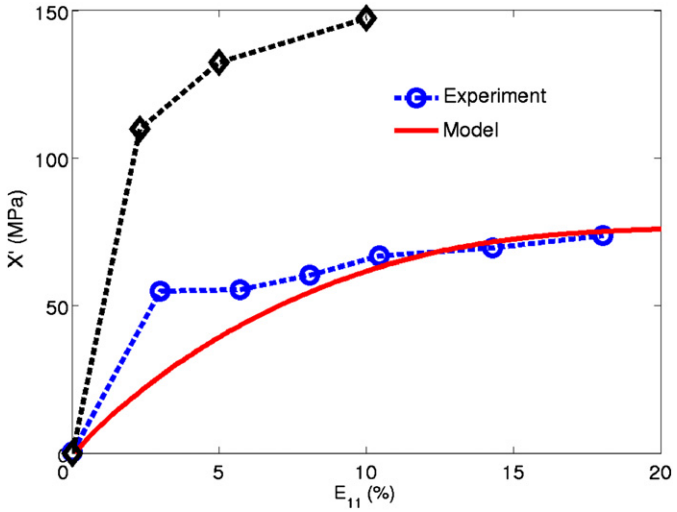

Fig. 13. Bauschinger stress X' model predictions (bold line) by using ILMF reference stress curves of Fig. 10, and experimental estimations (circles) by using both phase stresses of Fig. 8. The experimental Bauschinger stress X reported in Fig. 4 and derived from the macroscopic data in Fig. 3 is also reported (diamonds).

where f_C=5.7%. Eq. (15) arises naturally from internal stress self-equilibrium in the considered two-phase composite [37]. In Fig. 13, we compared the values given by Eq. (15) for X' and the ones given by Fig. 4 for X. To compute X', we used the phase stresses predicted by the ILMF model. The results are consistent with the values for X' calculated from experimental phase stress estimations of Fig. 8. Remarkably, the saturation of the Bauschinger effect with increasing strain is captured by the model, and is here explained by the saturation of isotropic strain hardening in ferrite. However, it is noteworthy that the macroscopic Bauschinger stress X is about twice higher than the model predictions for X'.

The overall Bauschinger effect (X) is indeed reinforced by the polycrystalline feature of the steel and the presence of GNDs at ferrite–ferrite grain boundaries [13], which also produce intra-phase backstress. Experimental values for the Bauschinger stress are reported in Ref. [34] in the case of reversible shear tests in pure ferritic steels (without cementite particles) for similar grain size. Hence, the additive effects of large GND densities near ferrite–ferrite interfaces close the difference between X and X' for the present steel.

5. Conclusions

A ferrite–cementite steel was first specifically designed to calibrate and validate an Internal Length Mean Field (ILMF) model first introduced in Ref. [14].

To achieve this objective, in situ tensile experiments combined with XRD and Synchrotron diffraction lattice strain measurements were performed to derive the average stress evolutions in both ferrite and cementite during tensile loading.

In addition to the macroscopic tensile stresses, these stresses were used to calibrate the thickness λ of an intermediate layer "phase" with large GND density between ferrite and cementite particles through the ILMF model.

A layer thickness of 0.3 μm was found to give reasonable estimate of the important difference between the stresses in ferrite and cementite found by lattice strain measurements. Without this GND layer and its contribution to isotropic hardening by dislocation tangles, the large difference between phase stresses cannot be reproduced by the model. The aspect ratio of particles was also shown to have an impact on this difference.

In addition to previous unit cell FDM simulations performed on another particulate-reinforced alloy in Ref. [14], experimental tension–compression tests were also performed to validate the value of λ regarding the overall Baushinger stress.

The measured Bauschinger stress as a function of forward prestraining is reasonably predicted from the phase stresses predicted by the ILMF model during first stage tensile loadings.

In particular, the saturation of the Bauschinger stress with forward tensile strain is captured.

For future study, the polycrystalline aspect with physical mechanisms taken into account at the scale of slip systems should be developed for a better quantitative description of the overall experimental Bauschinger effect [38].

Acknowledgments

The authors are grateful to the "Agence Nationale de la Recherche (ANR)" under contract ANR-07-MAPR-0023 ("Cat-Size") for financial support. They are also thankful to Aleksei Bytchkov and Jon Wright from ESRF, ID11 beamline, for their invaluable advice on ring diffraction.

Appendix A

A.1 XRD and ring diffraction experimental device

Both X-Ray Diffraction (XRD) and synchrotron radiation were used to obtain the per phase stress distribution in the designed steel during in situ uniaxial tensile tests at room temperature when applying increasing stress until failure. These non-destructive techniques were used to determine the average stress in both metallurgical phases: bcc ferrite and orthorhombic cementite. First, a small micromachine was directly placed under a PROTO iXRD goniometer equipped with a chromium anticathode. The average macroscopic stress and strain were recorded with load and displacement cells, respectively. In accordance with the European standard, the $\sin^2\psi$ method was used to follow only the stress evolution in ferrite (surface analysis), considering the {211} planes (2θ=156.1°). Because of the low volume fraction of cementite, the level of stress in this phase could not be assessed during these tests. The same in situ tensile tests were then carried out at the European Synchrotron Radiation Facility (ESRF, ID11 beamline) with high-energy X-rays. Ring diffraction measurements were performed with a 60 keV (λ=0.207 Å) monochromatic X-ray beam in transmission mode to follow the evolution of the bulk stress in both ferrite and cementite simultaneously.

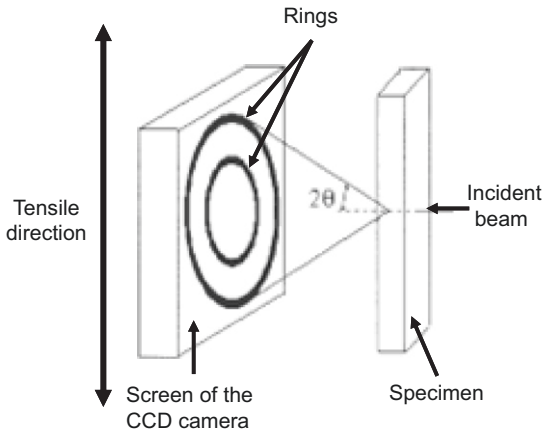

Fig. A1. Ring diffraction device in the ESRF-ID11 beamline [39].

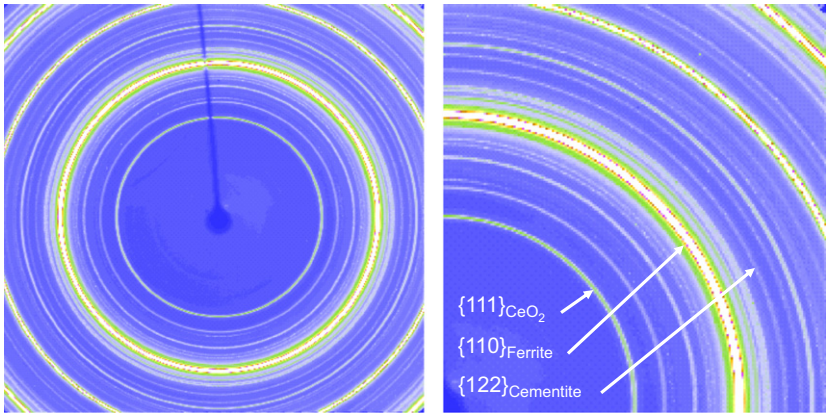

Fig. A2. Ring diffraction pattern with different rings corresponding to the two phases of the material analyzed and the CeO_2 calibrant.

The stress analyses in cementite were possible because both the X-ray flux and the diffracting volume are higher than those of lab XRD. A schematic representation of the experimental device is shown in Fig. A1 [16]. The micromachine was placed in such a way that the tensile axis was always vertical. The different specimens were previously covered with a thin layer of vacuum grease and a nanocrystalline CeO_2 cerium dioxide powder as a calibrant. The 1 mm^2 incident beam entered normally to the specimens forming complete Debye–Scherrer rings from ferrite, cementite and the CeO_2 calibrant. These resulting 2D diffraction rings were recorded by a Frelon 2D CCD camera with a resolution of 2048×2048 pixels and a 48.1×46.8 µm pixel size. The sample-to-camera distance was 340 mm in order to focus mainly on the {110} planes of ferrite and the {122} planes of cementite. These ones were chosen because their corresponding ring was relatively "isolated" from the others at this distance.

A.2. Diffraction analysis

The XRD $\sin^2\psi$ method was used in a classical way to follow the evolution of the stress in the ferritic phase [39]. Thirteen ψ angles were tested for each analysis to determine the σ_φ stress values only in the tensile direction. The elastic strain was first calculated for each ψ angle as follows:

$$\varepsilon = \frac{d-d_0}{d_0} \tag{A1}$$

where d_0 and d are the interreticular spacings of the considered planes respectively for the unstressed material and during loading. The final stress σ_φ is then deduced from the $\sin^2\psi$ method

$$\varepsilon_{\varphi\psi} = \frac{1+\nu}{E}\sin^2\psi\sigma_\varphi - \frac{\nu}{E}Tr(\sigma) \tag{A2}$$

where E and ν are respectively the macroscopic Young's modulus and the Poisson ratio of the material.

A typical pattern of ring diffraction is shown in Fig. A2. In this figure, the most intense rings correspond to ferrite. The others are due to cementite and CeO_2 while the darker beam stop is visible in the center of the pattern. Many peaks are observed especially for cementite due to its orthorhombic structure. However, most of them are double peaks, corresponding to two different plane families diffracting at the same 2θ position, or are peaks very close to each other. Hence, that makes them very difficult to analyze precisely in particular when peaks are becoming wider during loading. Therefore, in order to limit the resulting uncertainties in stress determination, this work was mainly focused on {111} planes of CeO_2 (for the calibration of the rings) and on {110} planes of ferrite as well as {122} planes of cementite. The FIT2D software [19] was used to determine all the geometrical parameters of the experiments for each pattern. The first four CeO_2 rings were considered for the position of the beam center, the tilt angle and the sample-to-detector distance. The (elastic) lattice strain component ε^e_{11} (resp. ε^e_{22}) obtained in the tensile (resp. transverse) direction was calculated by integrating only the corresponding part of the rings. Since the tensile direction was vertical, two different masks (vertical and horizontal) were created for this purpose. The resulting peaks of all phases were intense enough to determine precisely the corresponding 2θ diffraction angle (profile fitting). The different elastic strain components were finally given by Eq. (A1).

References

[1] J.P. Mathieu, K. Inal, S. Berveiller, O. Diard, J. Nucl. Mater. 406 (2010) 97–112.
[2] R. Hill, J. Mech. Phys. Solids 13 (1965) 89–101.
[3] M. Berveiller, A. Zaoui, J. Mech. Phys. Solids 26 (1979) 325–344.
[4] G. Cailletaud, P. Pilvin, Rev. Eur. Elem. Finis 3 (1994) 515–541.
[5] S. Berbenni, M. Berveiller, T. Richeton, Int. J. Solids Struct. 45 (2008) 4147–4172.
[6] C.W. Nan, D.R. Clarke, Acta Mater. 44 (1996) 3801–3811.
[7] M.F. Ashby, Philos. Mag. 21 (1970) 399–424.
[8] O. Bouaziz, Y. Bréchet, Scr. Mater. 60 (2009) 366–368.
[9] F.J. Humphreys, Acta Metall. 27 (1979) 1801–1814.
[10] L.M. Brown, W.M. Stobbs, Philos. Mag. 23 (1971) 1185–1233.
[11] D.A. Korzekwa, D.K. Matlock, G. Krauss, Metall. Trans. A 15 (1984) 1221–1228.
[12] M. Calcagonotto, D. Ponge, E. Demir, D. Raabe, Mater. Sci. Eng. A 527 (2010) 2738–2746.
[13] N. Allain-Bonasso, F. Wagner, S. Berbenni, D.P Field, Mater. Sci. Eng. A 548 (2012) 56–63.
[14] V. Taupin, S. Berbenni, C. Fressengeas, O. Bouaziz, Acta Mater. 58 (2010) 5532–5544.
[15] H.J. Chang, A. Gaubert, M. Fivel, S. Berbenni, O. Bouaziz, S. Forest, Comput. Mater. Sci. 52 (2012) 33–39.
[16] B.B. He, Two-dimensional X-ray Diffraction, Wiley, Hoboken, NJ, 2009.
[17] R. Sowerby, D.K. Uko, Y. Tomita, Mater. Sci. Eng. 41 (1979) 43–58.
[18] K. Van Acker, J. Root, P. Van Houtte, E. Aernoudt, Acta Mater. 44 (1996) 4039–4049.
[19] M.L. Young, J.D. Almer, M.R. Daymond, D.R. Haeffner, D.C. Dunand, Acta Mater. 55 (2007) 1999–2011.
[20] M.A. Weisser, A.D. Evans, S. Van Petegem, S.R. Holdsworth, H. Van Swygenhoven, Acta Mater. 59 (2011) 4448–4457.
[21] H. Mecking, U.F. Kocks, Acta Metall. 29 (1981) 1865–1875.
[22] A. Acharya, A.J. Beaudoin, J. Mech. Phys. Solids 48 (2000) 2213–2230.
[23] P. Suquet, in: P. Suquet (Ed.), CISM Lectures Notes, vol. 377, Springer-Verlag, Wien, 1997, pp. 197–264.
[24] J.-L. Chaboche, P. Kanouté, C. R. Méc. 331 (2003) 857–864.
[25] A. Rekik, F. Auslender, M. Bornert, A. Zaoui, Int. J. Solids Struct. 44 (2007) 3468–3496.
[26] R.M. Christensen, K.H. Lo, J. Mech. Phys. Solids 27 (1979) 315–330.
[27] E. Hervé, A. Zaoui, Eur. J. Mech. A: Solids 9 (1990) 505–515.
[28] E. Hervé, A. Zaoui, Int. J. Eng. Sci. 31 (1993) 1–10.
[29] V. Marcadon, E. Hervé, A. Zaoui, Int. J. Solids Struct. 44 (2007) 8213–8228.
[30] M. Cherkaoui, H. Sabar, M. Berveiller, J. Eng. Mater. Technol. 116 (1994) 274–278.
[31] S. Berbenni, M. Cherkaoui, Philos. Mag. 90 (2010) 3003–3026.
[32] R. Hill, J. Mech. Phys. Solids 31 (1983) 347–357.

[33] H. Ledbetter, Mater. Sci. Eng. A 527 (2010) 2657–2661.
[34] J.-M. Pipard, N. Nicaise, S. Berbenni, O. Bouaziz, M. Berveiller, Comput. Mater. Sci. 45 (2008) 604–610.
[35] T. Richeton, G.F. Wang, C. Fressengeas, J. Mech. Phys. Solids 59 (2011) 2023–2043.
[36] V. Taupin, S. Berbenni, C. Fressengeas, Acta Mater. 60 (2012) 664–673.
[37] S. Allain, O. Bouaziz, Mater. Sci. Eng. A 496 (2008) 329–336.
[38] B. Fournier, M. Sauzay, A. Pineau, Int. J. Plast. 27 (2011) 1803–1816.
[39] V. Hauk, Structural and Residual Stress Analysis by Nondestructive Methods, Elsevier Science B.V., Amsterdam, 1997.